LAWRENCE
LIVERMORE
NATIONAL
LABORATORY

Characterizing Turbulent Combustion Fields in Explosions

A. L. Kuhl, J. B. Bell, V. E. Beckner, K. Balakrishnan

November 9, 2011

Disclaimer

This document was prepared as an account of work sponsored by an agency of the United States government. Neither the United States government nor Lawrence Livermore National Security, LLC, nor any of their employees makes any warranty, expressed or implied, or assumes any legal liability or responsibility for the accuracy, completeness, or usefulness of any information, apparatus, product, or process disclosed, or represents that its use would not infringe privately owned rights. Reference herein to any specific commercial product, process, or service by trade name, trademark, manufacturer, or otherwise does not necessarily constitute or imply its endorsement, recommendation, or favoring by the United States government or Lawrence Livermore National Security, LLC. The views and opinions of authors expressed herein do not necessarily state or reflect those of the United States government or Lawrence Livermore National Security, LLC, and shall not be used for advertising or product endorsement purposes.

Characterizing Turbulent Combustion Fields in Explosions[‡]

Allen L. Kuhl

Lawrence Livermore National Laboratory, Livermore, CA

kuhl2@llnl.gov

John B. Bell, Vincent E. Beckner and Kaushik Balakrishnan

Lawrence Berkeley National Laboratory, Berkeley, CA

{jbbell, vebeckner, kaushikb}@lbl.gov

Abstract

Uncertainties in explosions are a consequence of turbulence effects on the flow. In this study, we quantify such uncertainties by evaluating the mean and fluctuating fields from implicit Large-Eddy Simulations (iles) of turbulent combustion in unconfined explosions. Two charge configurations are considered: a 0.5-g spherical PETN booster surrounded by a spherical shell of either 1-g of TNT solid or of 1-g of Aluminum (Al) powder; these provide the fuel for the combustion process. Detonation of booster disperses the fuel, whose expansion drives a blast wave into the surrounding atmosphere. The fuel-air interface is unstable and rapidly evolves into a turbulent mixing layer. The hot detonation products and the shock-heated air serve as ultra-strong ignition sources of the fuel-air mixture, which evolves into a spherical combustion cloud. The evolution of the blast wave and ensuing combustion cloud dynamics are studied via numerical simulations with our two-phase Adaptive Mesh Refinement (AMR) combustion code. The temperature field showed that combustion occurs along thin flame sheets for the TNT cloud, while a distributed-combustion mode is realized for the Al-powder case due to two-phase flow effects. Fuel consumption was limited to ~ 60% due to inherent limitations of turbulent entrainment of air into the cloud. We take advantage of the point symmetry in spherical blast waves, and azimuthally average the flow field to extract the mean and rms fluctuations from the turbulent fields. Thus we were able study the evolution of both the mean and rms profiles of the thermodynamic fields (pressure, temperature and density), the kinematic fields (velocity, Reynolds stress, kinetic energy and enstrophy), and the reaction zone profiles.

1. Introduction

This study investigates combustion clouds embedded in unconfined spherical explosions. Two charge configurations are considered: a 0.5-g spherical PETN booster surrounded by a spherical shell of either 1-g of TNT solid or of 1-g of Aluminum (Al) powder; these provide the fuel for the combustion process. Detonation of booster disperses the fuel, whose expansion drives a blast wave into the surrounding atmosphere. The fuel-air interface is unstable and rapidly evolves into a turbulent mixing layer. The hot detonation products and the shock-heated air serve as ultra-strong ignition sources of the fuel-air mixture, which evolves into a spherical combustion cloud [1,2]. The evolution of the blast wave and ensuing combustion cloud dynamics are studied via numerical simulations with our two-phase Adaptive Mesh Refinement (AMR) combustion code [3,4,5].

2. Model

2.1 Conservation Laws

The Model is based on the Eulerian multi-phase conservation laws for a dilute heterogeneous continuum, as formulated by Nigmatulin [6]. We model the evolution of the gas phase combustion fields in the limit of large Reynolds and Peclet numbers, where effects of molecular diffusion and heat conduction are negligible. The flow field is governed by the gas-dynamic conservation laws:

Mass: $\qquad \partial_t \rho + \nabla \cdot (\rho\, \mathbf{u}) = \dot{\sigma}_s$ (1)

Momentum: $\qquad \partial_t \rho \mathbf{u} + \nabla \cdot (\rho \mathbf{u}\mathbf{u} + p) = \dot{\sigma}_s \mathbf{v} - \dot{f}_s$ (2)

Energy: $\qquad \partial_t \rho E + \nabla \cdot (\rho \mathbf{u} E + p\mathbf{u}) = -\dot{q}_s + \dot{\sigma}_s E_s - \dot{f}_s \cdot \mathbf{v}$ (3)

where ρ, p, u represent the gas density, pressure and specific internal energy, $\mathbf{u}$ is the gas velocity vector, and $E \equiv u + \mathbf{u} \cdot \mathbf{u}/2$ denotes the total energy of the gas phase. Source terms on the right hand side take into account: mass addition to gas phase due to particle burning ($\dot{\sigma}_s$), particle drag ($\dot{f}_s$), and heat losses ($\dot{q}_s$).

We treat the particle phase as a Eulerian continuum field [6]. We consider the dilute limit, devoid of particle-particle interactions, so that the pressure and sound speed of the particle phase are zero. We model the evolution of particle phase mass, momentum and energy fields by the conservation laws of continuum mechanics for heterogeneous media:

Mass:
$$\partial_t \sigma + \nabla \cdot \sigma \, \mathbf{v} = -\dot{\sigma}_s \tag{4}$$

Momentum:
$$\partial_t \sigma \, \mathbf{v} + \nabla \cdot \sigma \, \mathbf{v}\mathbf{v} = -\dot{\sigma}_s \mathbf{v} + \dot{f}_s \tag{5}$$

Energy:
$$\partial_t \sigma e_s + \nabla \cdot \sigma \, e_s \mathbf{v} = \dot{q}_s - \dot{\sigma}_s e_s \tag{6}$$

where σ and $\mathbf{v}$ represent the particle-phase density and velocity, and $e_s = c_s T_s$ denotes the total energy of the particle phase.

2.2 Interactions

The inter-phase interaction terms for mass, momentum, heat and particle burning law take the form as described by Veyssiere and Khasainov [7]:

Mass Exchange:
$$\dot{\sigma}_s = \begin{cases} 0 & T_s < T_L \\ -3\sigma(1 + 0.276\sqrt{Re_s})/t_s & T_s \geq T_L \end{cases} \tag{7}$$

Momentum Exchange:
$$\dot{f}_s = \frac{3}{4} \frac{\rho}{\rho_s} \frac{\sigma}{d_s} C_D (\mathbf{u} - \mathbf{v}) |\mathbf{u} - \mathbf{v}| \tag{8}$$

Drag Coefficient:
$$C_D = 24/Re_s + 4.4/\sqrt{Re_s} + 0.42 \text{ and } Re_s = \rho d_s |\mathbf{u} - \mathbf{v}|/\mu \tag{9}$$

Heat Exchange:
$$\dot{q}_s = \frac{6\sigma}{\rho_s d_s} \left[\frac{Nu\lambda(T - T_s)}{d_s} + \varepsilon\sigma_{Boltz}(T^4 - T_s^4) \right] \tag{10}$$

Convective Heat Transfer:
$$Nu = 2 + 0.6\Pr\sqrt{Re_s} \tag{11}$$

Ingignoli Burning Law (1999):
$$t_s = Kd_s^2/\phi^{0.9} \tag{12}$$

2.3 Combustion

We consider three fuels: PETN detonation products (F_1), TNT detonation products (F_2) and Aluminum (F_3), and their corresponding combustion products: PETN-air (P_1), TNT-air (P_2), and Al-air (P_3). We model the combustion of fuel F_k with air (A) yielding equilibrium products P_k:

$$F_k + A \Rightarrow P_k \qquad (k = 1 \text{ or } 2 \text{ or } 3) \tag{13}$$
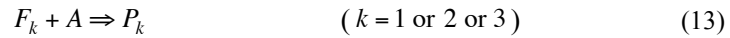
The mass fractions Y_k of the components are governed by the following conservation laws:

Fuel-k:
$$\partial_t \rho Y_{Fk} + \nabla \cdot \rho Y_{Fk} \mathbf{u} = -\dot{s}_k + \delta_{k2}\dot{\sigma}_k \tag{14}$$

Air:
$$\partial_t \rho Y_A + \nabla \cdot \rho Y_A \mathbf{u} = -\sum_k \alpha_k \dot{s}_k \tag{15}$$

Products-k:
$$\partial_t \rho Y_{Pk} + \nabla \cdot \rho Y_{Pk} \mathbf{u} = \sum_k (1 + \alpha_k)\dot{s}_k \tag{16}$$

Fuel and air are consumed in stoichiometric proportions: $\alpha_k = A/F_k$. In the above, $\dot{s}_k$ represents the global kinetics sink term. In this work we use the fast-chemistry limit that is consistent with the inviscid gas-dynamic model (1)-(3), so whenever fuel and air enter a computational cell, they are consumed in one time step. Here δ_{k2} represents the Kronecker delta ($\delta_{k2} = 0$ if k=1 and $\delta_{k2} = 1$ if k=2) and takes into account the vaporization of Al fuel from the particle phase EQ. (4), which creates a source of Al fuel in the gas phase.

2.4 Equations of State

Our code carries the density and specific internal energy, along with the gas composition in each cell. These are used to calculate the pressure and temperature in a computational cell based on Equations of State (EOS). The thermodynamic states encountered during SDF explosions have been analyzed in [8]. Here we summarize only the salient features needed for the numerical modeling. The caloric equation of state can be specified in the *Le Chatelier plane* of specific internal energy as a function of temperature: $u(T)$. Loci of states covering the temperature range $300\ K \leq T \leq 6{,}000\ K$ were calculated by the Cheetah code [9], based on the following thermodynamic assumptions:

- *Air:* equilibrium isobar[1] ($p = 10\ atm$)
- *Aluminum:* equilibrium isobar ($p = 10\ atm$)
- *PETN detonation products:* equilibrium isentrope passing through the Chapman-Jouguet point, with frozen composition for $T < 1{,}800\ K$ (see Rhee et al [10] for this formulation)
- *Al-air combustion products:* equilibrium isobar[4] ($p = 10\ atm$)

These loci were fit with piecewise quadratic functions for each component:

$$u(T) = aT^2 + bT + c \tag{36}$$

The coefficient values a,b,c are tabulated in [8]. Given the cell specific internal energy, u, temperature is evaluated by solving the above quadratic for T:

$$T = [-b + \sqrt{b^2 - 4a(c-u)}\,]/2a \tag{37}$$

Pressure is then calculated from the perfect gas relation[2]:

$$p = \rho R T \tag{38}$$

or from the JWL function in the detonation products gases:

$$p_{JWL}(v,T) = A\left(1 - \frac{\omega v_0}{R_1 v}\right)e^{-R_1 v/v_0} + B\left(1 - \frac{\omega v_0}{R_2 v}\right)e^{-R_2 v/v_0} + RT/v \tag{39}$$

where v is the specific volume ($v = 1/\rho$). For more details, see [8].

2.5 Numerical Methods

The above conservation laws were integrated with a high-order generalization of Godunov's method [11]. The algorithm is based on an efficient Riemann solver for gasdynamics first developed by Colella and Glaz [12] and Colella and Woodward [13] and extended to generalized conservation laws by Bell et al. [14] and to un-split upwind schemes by Colella [15]. The same high-order Godunov algorithm is applied to both the gas phase and the particle gas phase (with appropriate change in variables). Source terms are treated with Strang-splitting methods. Since the integrators are based on Riemann solvers; information propagates along characteristics at the correct wave speeds, and they incorporate nonlinear wave interactions within the cell during the time step. They include a limiting step (slope flattening) that automatically reduces the order of approximation in the neighborhood of discontinuities, while in smooth regions of the flow the scheme is second order in time and space.

The Godunov algorithm forms the integrator for our adaptive mesh refinement (AMR) code. Our adaptive methods are based on the block-structured AMR algorithms of Berger & Colella [16], and extended to three-dimensional hyperbolic systems by Bell et al. [17]. Embedded boundary methods [18] are used to represent irregular geometries. In this approach, regions to be refined are organized into rectangular patches, with several hundred to several thousand grid-points per patch. One can refine on discontinuities (shocks and contact surfaces), on Richardson error estimates, or for present purposes, on reaction zones. Grid patches are assigned to processors by a

---

[1] We found that the $u(T)_{isobar} = u(T)_{isochor}$ for $T < 3{,}500\ K$, hence it was sufficient to fit the internal energy as solely a function of temperature; above 3,500 K this is an approximation, accurate within < 10% error.
[2] We found this to be true for constant volume explosions for $p \leq 1\ kbar$

knapsack algorithm based on workload estimates, [19] so the AMR code runs efficiently on massively-parallel computers. [20]

AMR is also used to refine turbulent mixing regions; by successive refinements we are able to capture the energy-bearing scales of the turbulence on the computational grid. In this way we are able to compute the effects of turbulent mixing without resorting to explicit turbulence modeling. This is consistent with the so-called *MILES* (Monotone Integrated Large-Eddy Simulation) approach of Boris [21]. A comprehensive review of such implicit Large-Eddy Simulation (*iLES*) methods may be found in Grinstein et al [22]. Verification of the ability of our Godunov scheme to produce velocity fields that replicate the Kolmogorov spectrum of turbulent flow, has been demonstrated by Aspden et al [23].

3. Results

3.1 Flow Visualization

Turbulent combustion inside the cloud is visualized by a color-bar representation of the temperature field in Fig. 1. The TNT-air cloud reaches a combustion temperature of ~ 2,000 K, while the Al-air cloud reaches a combustion temperature between 3,000 and 4,000 K. For the TNT case, combustion occurs along thin flame sheets (Fig. 2), while a distributed-combustion mode is realized for the Al-powder case (Fig. 1 d-f) due to two-phase flow effects. By performing reactive and non-reactive flow simulations shown in Fig. 3, it was demonstrated that combustion caused no change in the pressure field during the positive phase of the blast wave—in other words, combustion in the fireball is isobaric.

3.2 Fuel Consumption

Fuel consumption histories are depicted in Fig. 4. In the unconfined cases, there is a limit as to how much air the spherical mixing layer can entrain before the turbulent velocity field dies. So the fuel consumption was limited to ~ 60%. In the confined cases, fuel consumption approached 100% due to the continued mixing induced by shock reverberations in the chamber [3],[4].

3.3 Azimuthal Averaging

We take advantage of the point symmetry inherent in spherical blast waves and azimuthally average the flow field to extract the *mean* and *rms* profiles from the numerical solution. Recall that the flow field $\Phi(x,y,z,t)$ is computed and stored at cell-centered points $P(x,y,z)$ on a Eulerian grid. The points are transformed to points $P(r,\theta,\phi)$ on a corresponding spherical grid, by the trigonometric formulas:

$$|\mathbf{r}| = \sqrt{x^2 + y^2 + z^2} \quad \text{and} \quad \theta = Cos^{-1}(z/|\mathbf{r}|) \quad \text{and} \quad \phi = Tan^{-1}(y/x) \tag{22}$$

We consider spherical shell volume δV at radius R_n

$$\delta V = \left[\iint (R_n d\theta)(R_n \sin\theta d\phi)\right]\delta r = 4\pi R_n^2 \delta r \tag{23}$$

A shell thickness equal to the mesh size is assumed ($\delta r = \Delta$). We denote computational cells located within this shell volume by $P_n = P(R_n,\theta,\phi)$ and the corresponding flow field values by $\Phi_n = \Phi(R_n,\theta,\phi,t)$. We then average the flow field at fixed R_n to evaluate the *mean* field:

Mean: $$\overline{\Phi(R_n,t)} = \frac{1}{\delta V(R_n)} \iiint_{\delta V} \Phi(R_n,\theta,\phi,t)dV \equiv \frac{1}{N}\sum_{n=1}^{N}\Phi_n \tag{24}$$

The ensemble size is $N = 4\pi(R_n/\Delta)^2 \sim 10^5$, except near the origin (see Table 1). Given the mean, one can then compute root-mean-squared (*rms*) fluctuations about the *mean*:

Fluctuation: $$\overline{\Phi'(R_n,t)^2} = \frac{1}{\delta V(R_n)} \iiint_{\delta V} [\Phi(R_n,\theta,\phi,t) - \overline{\Phi(R_n,t)}]^2 dV \equiv \frac{1}{N}\sum_{n=1}^{N}[\Phi_n - \overline{\Phi(R_n,t)}]^2 \tag{25}$$

rms: $$\Phi'(R_n,t)_{rms} \equiv \sqrt{\overline{\Phi'(R_n,t)^2}} \tag{26}$$

These were used to construct the evolution of the *mean* and *rms* profiles of the combustion cloud.

Table 1. Ensemble size, N^*

R_n	$N = 4\pi (R_n / \Delta)^2$
1	2,000
5	0.5×10^5
10	2×10^5
15	4.6×10^5
20	8×10^5

* for $\Delta_2 0.8 mm$

3.4 Thermodynamic Profiles

The azimuthally averaged thermodynamic profiles of density, temperature and pressure are presented in Fig. 5. The *mean* fields (left column) depict the one-dimensional blast wave fields engendered by the detonation of the TNT charge (*vid.* Brode[24,25]). The *rms* fields quantify the consequences of the three-dimensional turbulent mixing. Since pressure fluctuations are very small (~ 1% of ambient), density fluctuations track temperature fluctuations, which increase in time due to combustion.

3.5 Kinematic Profiles

The azimuthally averaged kinematic profiles are presented in Figs. 6. The *mean* radial velocity profiles again resemble those from TNT charges.[13] The *rms* velocity-fluctuation profiles (u_r', u_θ', u_ϕ') are similar in magnitude; at 0.2 ms they peak at ~ 60 m/s and decay to ~ 5 m/s by 4 ms. Thus the turbulence is isotropic in this problem. The Reynolds stress profiles at $t = 0.65\,ms$ are depicted in Fig. 6e. This flow is dominated by the diagonal stresses (τ_{rr}, $\tau_{\theta\theta}$, $\tau_{\phi\phi}$) whose profiles are similar, while the cross terms ($\tau_{r\theta}$, $\tau_{r\phi}$, $\tau_{\theta\phi}$) are negligible. The enstrophy profiles $\omega^2(r,t)$ also decay with time, as shown in Fig. 6f.

3.6 Turbulent Kinetic Energy Decay

Evolution of the global kinetic energy: *KE(t)* and global fluctuating kinetic energy: *FKE(t)* are shown in Fig. 7. Decay of the kinetic energy is caused by the blast wave evolution. The steep decay at 2 ms signals that the blast wave has exited the computational domain. The decay of the fluctuating kinetic energy is related to the energy cascade of the turbulent flow. This contrasts with our previous two-dimensional (2D) simulations of this problem [26], where the *KE* approached a constant; the fluctuating kinetic energy did not decay because the energy cascade mechanism is absent in 2D flows.

3.7 Reaction Zone Profiles

The development of the component mass-fraction profiles: $Y_k(r,t)$ (where *k = D, DP, F, CP, A* representing PETN driver gas, PETN-air combustion products, TNT detonation products as a fuel, TNT-air combustion products and air, respectively) are presented in Fig. 8. Most prominently Fig. 8 shows the initiation and growth of the combustion products CP near $r = 10\,cm$, and the depletion of fuel: F and air: A due to combustion. Eventually the combustion products spread throughout the cloud (Fig. 8f) as a consequence of turbulent mixing.

4. Summary and Conclusions

The characteristic temperature in the TNT-air combustion cloud is around 2,000 K, while the temperature in the Al-air combustion cloud is between 3,000 K and 4,000 K. This trend is consistent with the adiabatic flame temperature of 2,900 K for stoichiometric TNT-air combustion and 4,120 K for stoichiometric Al-air combustion. Combustion occurs along thin flame sheets for the TNT case, while a distributed mode of combustion is observed for the Al-air case; the latter is attributed to a two-phase (slip-flow) effect.

In unconfined explosions, combustion is isobaric, and thus has no effect of the TNT blast wave pressure distribution. This finding has been confirmed by pressure measurements of such blast waves [5].

Fuel consumption was limited to ~ 60%. This corresponds to the amount of air that can be entrained into the cloud before the turbulent velocity field dies. This seems to be an inherent property (limit) of such spherical mixing layers. This contrasts with confined combustion in calorimeters, where fuel consumption was more that 90 % for the same fuels as a result of the continued mixing induced by shock reverberations in the chamber. [1, 2, 3]

Azimuthal averaging was used to extract the *mean* $\overline{\Phi(r,t)}$ and *rms* fluctuations $\Phi'(r,t)_{rms}$ from the numerical solution. This included thermodynamic profiles (of density, temperature and pressure), kinematic profiles

(of velocity, Reynolds stress and enstrophy) and reaction zone profiles. There were typically 10^5 samples in the ensemble of each spherical shell (except near the origin), so the resulting profiles were very smooth. We were able to extract such smooth profiles from a *single* numerical simulation by a propitious formulation of the problem (i.e., azimuthal averaging of a spherically-symmetric explosion).

Finally, the azimuthal averaging was used to study the evolution of the reaction zone in the TNT explosion. The mass-fraction profiles $Y_k(r,t)$ can be used to construct analytic models of the combustion layer.

Acknowledgements

References

[1] A. L. Kuhl, H. Reichenbach, Combustion effects in confined explosions, *Proc. Combustion Institute* **32** (2) pp. 2291-2298, 2009.

[2] A. L. Kuhl, H. Reichenbach, Barometric calorimeters, *Comb., Exp. & Shock Waves*, **4** (2) pp. 271-278, 2010.

[3] A. L. Kuhl, J. B. Bell, V. E. Beckner, Heterogeneous continuum model of aluminum particle combustion in explosions, *Combustion Explosion and Shock Waves* **46** (4), pp. 433-448, 2010.

[4] A. L. Kuhl, J. B. Bell, V. E. Beckner, H. Reichenbach, Gasdynamic model of turbulent combustion in TNT explosions, *Proc. Combustion Institute* **33** (II) pp. 2177-2185, 2010.

[5] A. L. Kuhl, H. Reichenbach, J. B. Bell, V. E. Beckner, Reactive blast waves from composite charges, *14th Int. Detonation Symposium*, Office of Naval Research ONR-351-10185 pp 806-815, 2011.

[6] R. I. Nigmatulin *Dynamics of multi-phase flows* Vol. 1, Moscow, Nauka, 464 pp., 1987.

[7] B. Veyssiere, B. Khasainov, A model for steady, plane, double-front detonations (DFD) in gaseous explosive mixtures with Al particles in suspension, *Combustion & Flame* **85** (1,2) pp. 241-253, 1991.

[8] A. L. Kuhl & B. Khasainov, Quadratic model of thermodynamic states in SDF explosions, *Energetic Materials: 38th Int. Conf. ICT* pp. 143.1-143.11, 2007.

[9] L. E. Fried, *CHEETAH 1.22 User's Manual*, Report No. UCRL-MA-117541, LLNL (1995).

[10] F. H. Ree, W. J. Pitz, M. van Thiel, P. C. Souers, "Over-abundance of Carbon Monoxide in Calorimeter Tests", *J. Phys. Chem*. 1996, **100**, pp. 5761-5765.

[11] van Leer, B. Towards the Ultimate Conservative Difference Scheme V: a Second-order Sequel to Godunov's Methods, *J Comp. Phys*., 32, 1979, pp. 101-136.

[12] Colella, P. & Glaz, H. M., Efficient Solution Algorithms for the Riemann Problem for Real Gases, *J Comp. Phys.,* **59**, 1985, pp. 264-289.

[13] Colella, P. & P. R. Woodward, P. R., The Piecewise Parabolic Method (PPM) for Gasdynamical Simulations, *J Comp. Phys*., 54, 1984, pp. 174-201.

[14] Bell, J. B., Colella, P. & Trangenstein, J. A., Higher Order Godunov Methods for General Systems of Hyperbolic Conservation Laws, *J Comp. Phys*., 92(2), 1989, pp. 362-397.

[15] Colella, P. "Multidimensional Upwind Methods for Hyperbolic Conservation Laws", *J Comp. Phys*., 87, 1990, pp. 171-200.

[16] Berger, M. J. & Colella, P. Local adaptive mesh refinement for shock hydrodynamics, *J Comp. Phys*., **82** (1), 1989, pp. 64-84.

[17] Bell, J., Berger, J. M., Saltzman, J., & Welcome, M., A Three-dimensional adaptive mesh refinement for hyperbolic conservation laws, *SIAM J. Sci. Statist. Comput.,* **15**(1), 1994, pp. 127-138.

[18] Pember, R. B., Bell, J. B., Colella, P., Crutchfield, W. Y., & Welcome, M. L., An Adaptive cartesian grid method for unsteady compressible flow in complex geometries, *J Comp. Phys*. 120 (2), 1995, pp. 278-304.

[19] Crutchfield, W. Y., & Welcome, M. L., Object-oriented Implementation of adaptive mesh refinement algorithms, *Scientific Programming*, 2, 1993, pp. 145-156.

[20] Rendleman, C. A., Beckner, V. E., Lijewski, M., Crutchfield, W. Y., & Bell, J. B., Parallelization of structured, hierarchical adaptive mesh refinement algorithms, *Computing and Visualization in Science*, Vol. 3, 2000.

[21] Boris, J. P., On large eddy simulations using sub-grid turbulence models, *Wither Turbulence? Turbulence at the Crossroads*, ed. J. L. Lumley, *Lecture Notes in Physics,* **257**, Springer-Verlag, Berlin, pp 344-353, 1989.

[22] Grinstein, F. F., Margolin, L. G., and Rider, W. J., Editors, *Implicit Large-Eddy Simulation: Computing Turbulent Fluid Dynamics*, Cambridge University Press, 546 pp., 2007.

[23] Aspden, A. J., Nikiforakis, N, Dalziel, S. B. & Bell, J. B., Analysis of implicit LES methods, *Comm. Applied Mathematics and Computational Science*, **3**, pp.103-126, 2008.

[24] Brode, H. L., *A Calculation of the Blast Wave from A Spherical Charge of TNT*, Rand Report **RM-1965**, Rand Corp., Santa Monica, 1957, 61 pp.

[25] Brode, H. L. Blast wave from a spherical charge, *Phys. Fluids*, **2**(2), pp. 217-229 (1959).

[26] Kuhl, A. L. Spherical mixing layers in explosions, *Dynamics of Exothermicity,* J. R. Bowen Ed., Gordon and Breach Publishers, Longhorn, Pennsylvania, pp. 290-320 (+ 2 color plates), 1996.

Figure 1. Cross-sectional view of the temperature field of spherical combustion clouds: frame *a-c* illustrate TNT-air combustion while frames *d-f* depict Al-air combustion (colors denote temperature — red: 3,000 < *T* < 4,000 K; yellow: *T* = 2,000 K; turquoise: T = 1,000 K).

(a) flow field   (b) blow-up near front
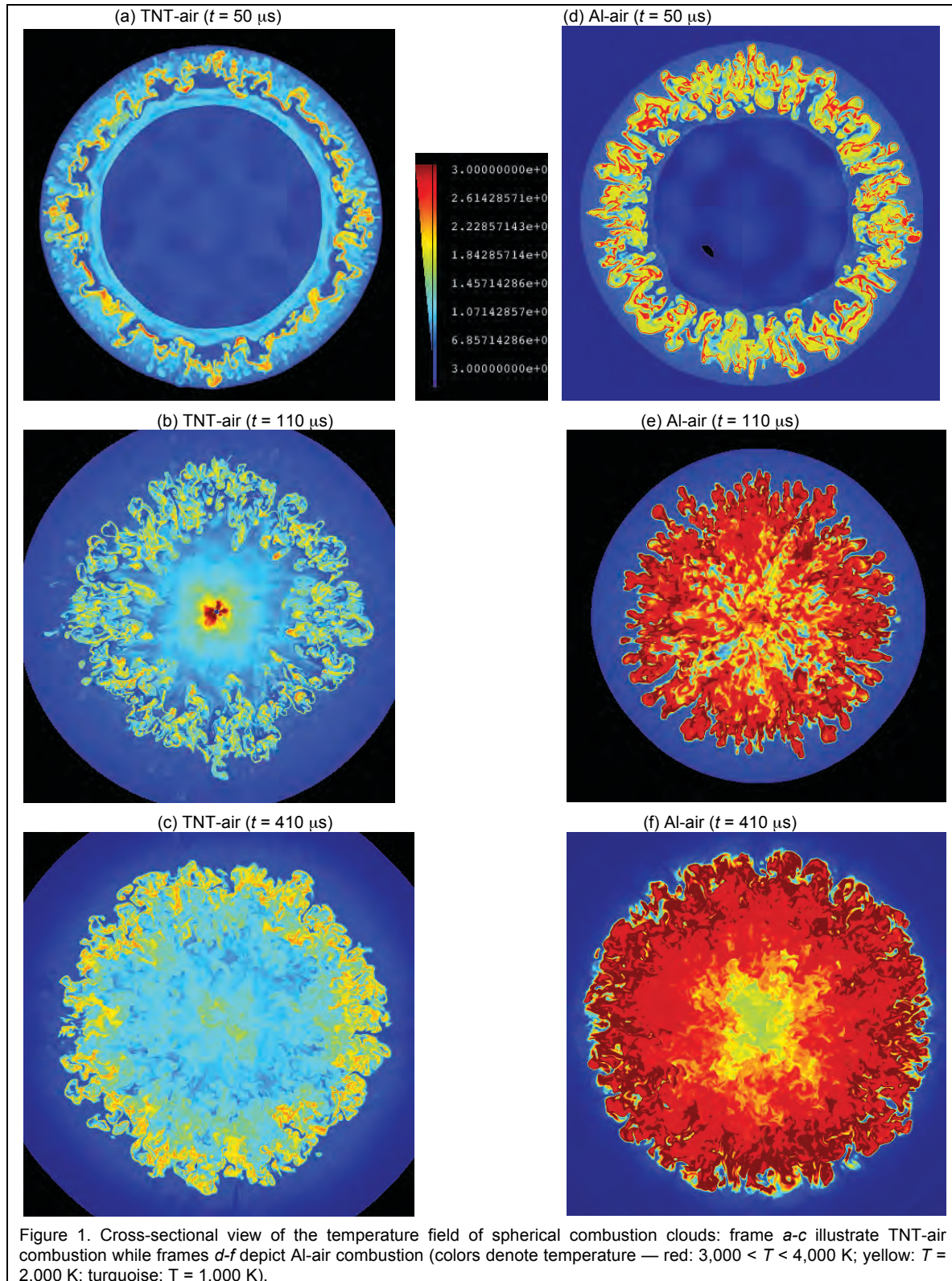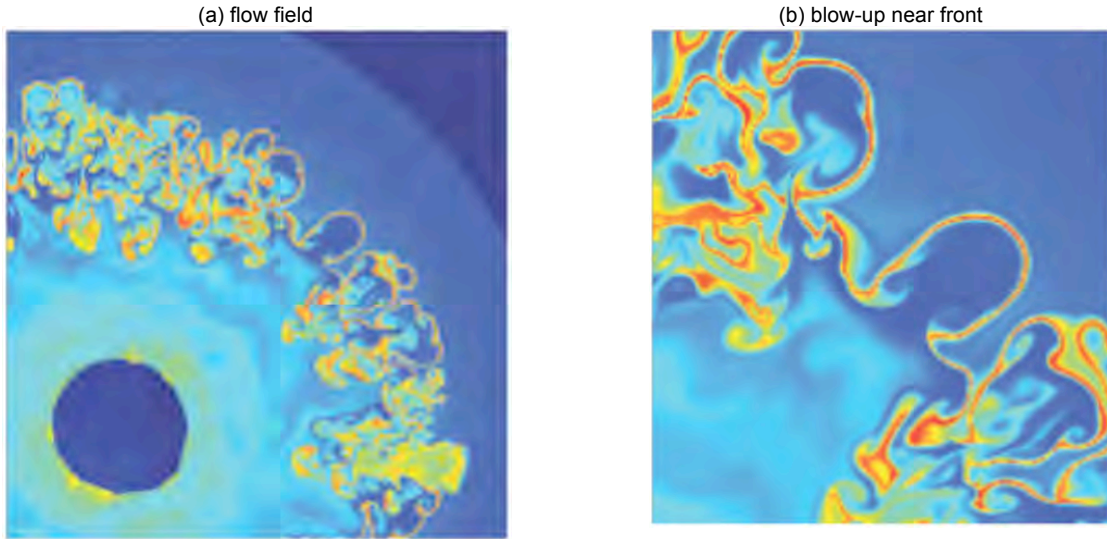
Figure 2. Exothermic flame sheet in the TNT-air combustion field (t = 100 μs).
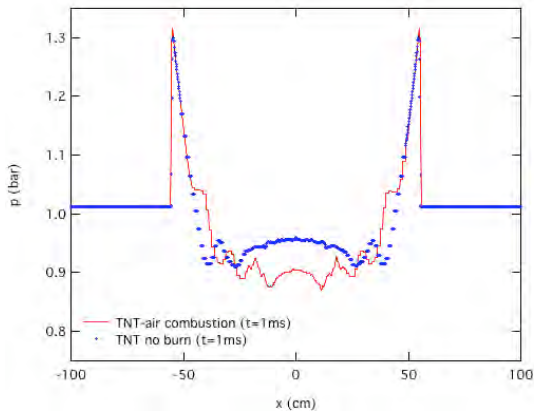
Figure 3. Blast wave pressure distribution $p(x, t = 1ms)$ along the *x-axis* at for TNT explosion in air: Notation: solid curve denotes combustion with air while dotted curve represents the no combustion case.
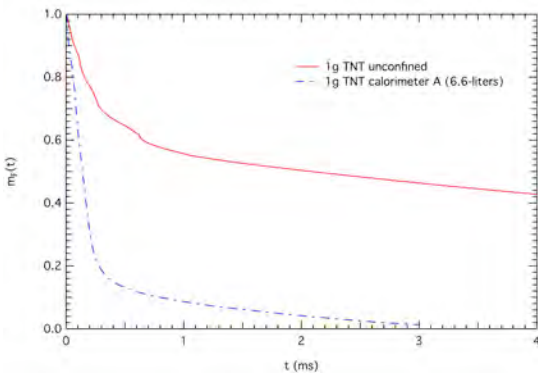
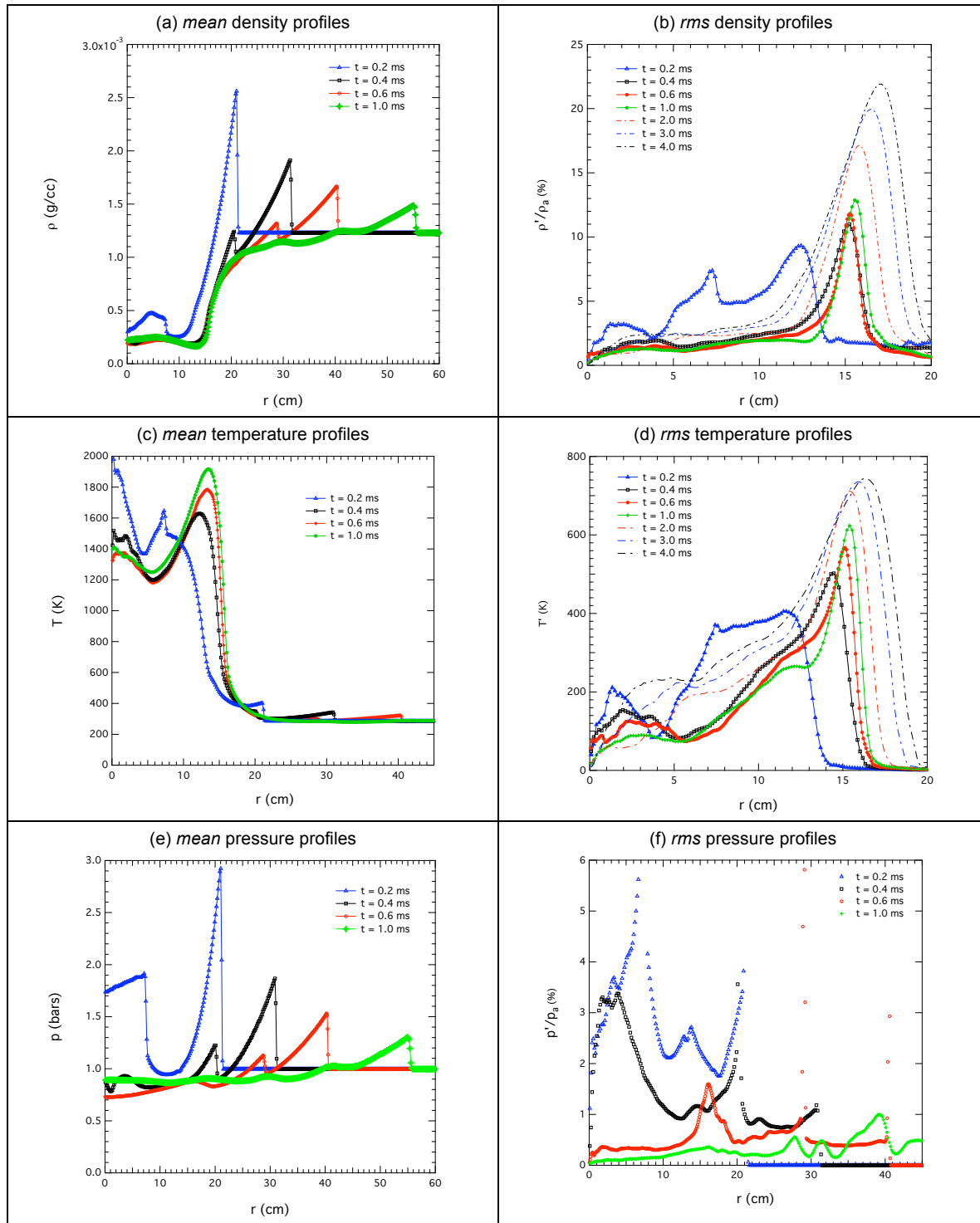Figure 4. Fuel consumption over time for TNT-air combustion

Figure 5. Evolution of the *mean* and *rms* thermodynamic profiles in the TNT combustion cloud.
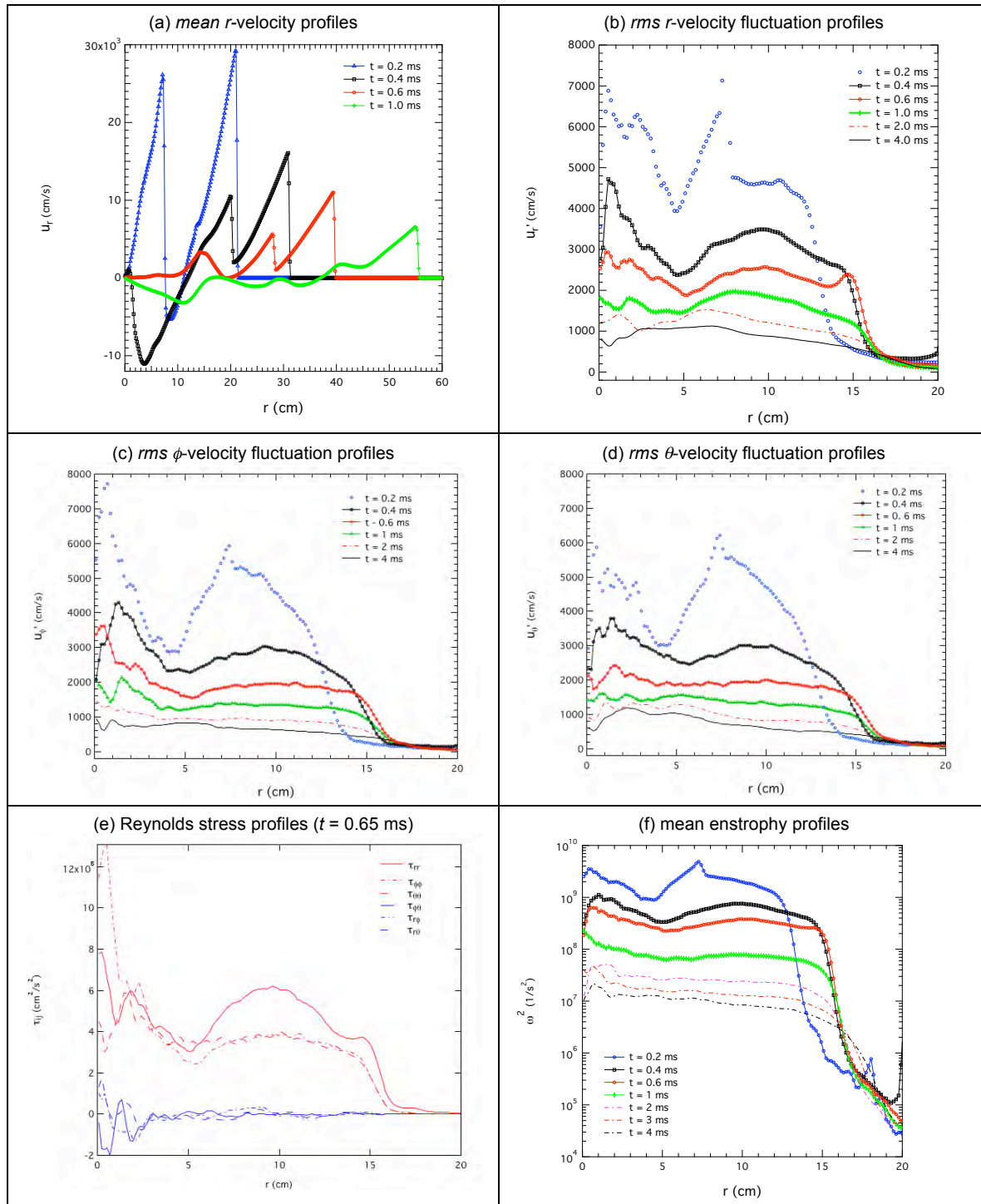
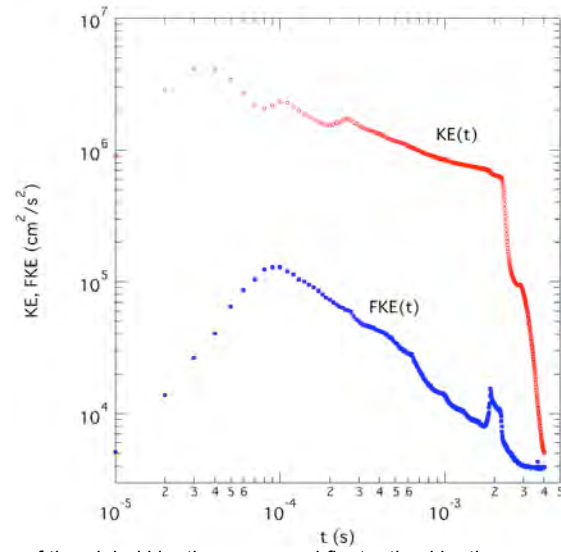Figure 6. Evolution of the *mean* and *rms* kinematics profiles in the TNT combustion cloud.

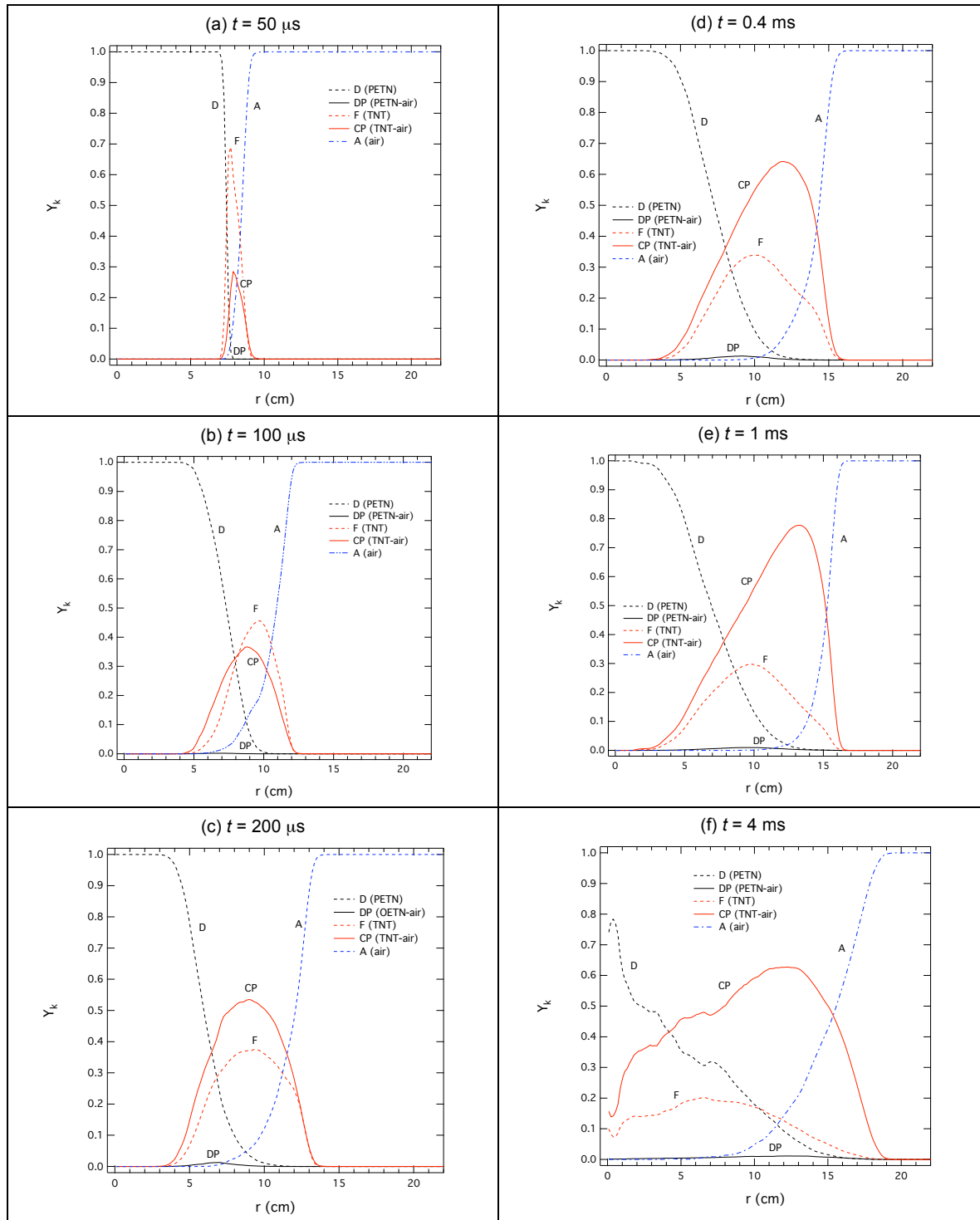Figure 7. Evolution of the global kinetic energy and fluctuating kinetic energy in the TNT explosion.

Figure 8. Evolution of the mean mass-fraction profiles $Y_k(r,t)$ in the combustion zone of the TNT cloud (Notation: D = PETN driver, DP = PETN-air combustion products, F = TNT fuel, CP = TNT-air combustion products, A = air).